

A modified invasion percolation model for low–capillary number immiscible displacements in horizontal rough-walled fractures: Influence of local in-plane curvature

Robert J. Glass

Flow Visualization and Processes Laboratory, Sandia National Laboratories, Albuquerque, New Mexico

Michael J. Nicholl

School of Geology, Oklahoma State University, Stillwater

Lane Yarrington

Flow Visualization and Processes Laboratory, Sandia National Laboratories, Albuquerque, New Mexico

Abstract. We develop and evaluate a modified invasion percolation (MIP) model for quasi-static immiscible displacement in horizontal fractures. The effects of contact angle, local aperture field geometry, and local in-plane interfacial curvature between phases are included in the calculation of invasion pressure for individual sites in a discretized aperture field. This pressure controls the choice of which site is invaded during the displacement process and hence the growth of phase saturation structure within the fracture. To focus on the influence of local in-plane curvature on phase invasion structure, we formulate a simplified nondimensional pressure equation containing a dimensionless curvature number (C) that weighs the relative importance of in-plane curvature and aperture-induced curvature. Through systematic variation of C , we find in-plane interfacial curvature to greatly affect the phase invasion structure. As C is increased from zero, phase invasion fronts transition from highly complicated (IP results) to macroscopically smooth. In addition, measurements of fracture phase saturations and entrapped cluster statistics (number, maximum size, structural complication) show differential response between wetting and nonwetting invasion with respect to C that is independent of contact angle hysteresis. Comparison to experimental data available at this time substantiates predicted behavior.

1. Introduction

Macroscopic effective properties that purport to describe the pressure-saturation, relative permeability, solute dispersivity, and fracture-matrix interaction behavior of a single fracture are functions of phase geometry within the fracture [*Glass et al.*, 1995b, 1996]. As a prelude to numerical construction of two-phase pressure-saturation and relative permeability relations for an individual fracture aperture field, standard percolation (SP), first introduced by *Broadbent and Hammersley* [1957], has been used to model phase structure as a function of pressure [e.g., *Pyrak-Nolte et al.*, 1990; *Pruess and Tsang*, 1990]. At a given pressure, local aperture within the simulated fracture aperture field (often spatially correlated) entirely determines whether that location is filled with the wetting or nonwetting phase. This approach for determining phase structure has been assumed relevant to low–capillary number flows where viscous forces are negligible compared to capillary forces (e.g., mobilization of entrapped phase ganglia does not occur). Results of the SP approach suggest that the two-dimensional nature of the aperture network increases the importance of phase interference and trapping.

Implicit in the application of SP is an assumption that all

apertures are in a state of mutual communication and at equilibrium within the system. For fractures, three communication processes exist, all of which are “non-aperture-spanning”: flow through the matrix that connects all apertures (wetting phase), film flow along the fracture walls (wetting phase), and diffusive-advective (transport of one phase within another) processes (both wetting and nonwetting phases). To satisfy equilibrium, timescales must be long with respect to those of the communication processes.

In a large number of situations where one phase within the fracture displaces the other, communication processes may not exist. Alternatively, displacement may occur at a rate that is orders of magnitude faster than communication processes, but still under quasi-static conditions where viscous forces are negligible. For these situations, accessibility of apertures to a phase, that is, adjacency of an aperture to a phase and connection within that phase to a source or sink, places an additional control on phase displacement geometry. Models which incorporate such accessibility rules for application to low–capillary number flows have been termed invasion percolation (IP), after the work of *Wilkinson and Willemsen* [1983]. Forms of IP have been applied to spatially correlated aperture fields by *Kwicklis and Healy* [1993] and *Mendoza* [1992] to calculate fracture pressure saturation and relative permeability relations.

Neither SP nor IP approaches adequately capture either the quantitative or qualitative character of small–capillary number

Copyright 1998 by the American Geophysical Union.

Paper number 98WR02224.
0043-1397/98/98WR-02224\$09.00

phase invasion structures measured experimentally in transparent analog fractures [e.g., Nicholl *et al.*, 1992, 1993a, b, 1994; Nicholl and Glass, 1994; Glass and Nicholl, 1995a, b]. With respect to predictions based on SP or IP approaches, these experiments, which were conducted in impermeable walled fractures, have demonstrated macroscopic fronts; decreased phase entrapment on invasion; and depressed wetting phase capillary rise, macroscopic gravity/buoyancy driven fingers, and compact entrapped phase dissolution. Furthermore, in experiments where the wetting phase entered the fracture from a surrounding matrix, invasion was observed to occur from discrete contact points [Glass and Norton, 1992]. Once initiated from these “nucleation” sites, invasion fronts have a similar character to those with no matrix influence.

In this paper we begin development of a modified invasion percolation (MIP) model that incorporates additional physics necessary to conform with experimental observations. At this stage, we focus on the importance of local interfacial geometry, and do not include viscous or gravitational forces, nor the non-aperture-spanning communication processes mentioned above. Both SP and IP implement a simplified aperture-induced curvature that assumes fracture walls are locally parallel. Accurate description of the local interfacial geometry requires us to also consider both the local convergence/divergence of the fracture walls, and the local curvature of the interface within the “plane” of the fracture (“in-plane” curvature, normal to the local aperture induced curvature). Glass [1993] included both these additional influences, along with gravitational forces to simulate gravity-driven fingers in fractures. While these early simulations showed reasonable qualitative and quantitative agreement with experimental observations, the rudimentary approach used for calculating in-plane curvature created artificially blocky structures oriented in the directions of the computational grid. Here, we implement a more versatile formulation for in-plane curvature within the MIP model. While still approximate and not without limitations, this formulation allows us to begin systematic study of how local interfacial geometry influences phase growth in fractures.

Full exploration of the local interfacial geometry’s influence on phase displacement in fractures is beyond the scope of this paper. After introducing the general model, we take the contact angle to be constant in time and space and assume that local convergence/divergence of the aperture field has a negligible influence. We then write a simplified nondimensional equation in which the relative magnitude of the two principle radii of curvature (in-plane and aperture-induced) are expressed as a dimensionless curvature number (C). We vary C systematically in simulations for both wetting and nonwetting invasion within a baseline dimensionless fracture aperture field that is statistically equivalent to those we have used in previous phase invasion experiments. We find that as C increases from 0 (the IP limit), the phase invasion structure transitions from highly complicated to macroscopically smooth. Inclusion of in-plane curvature allows us to model the experimentally observed macroscopic fronts, decreased phase entrapment on wetting versus nonwetting invasion, and compact entrapped phase dissolution for phase invasion at low capillary number in horizontal fractures.

2. Conceptual Model Development

Invasion percolation (IP), introduced by Wilkinson and Wilmsen [1983], models phase invasion on a network where the

pressure within each phase varies as a function of time, but not in space. This is a reasonable assumption in the limit of infinitesimal flow rate where viscous forces are negligible with respect to capillary forces (i.e., quasi-static flow at small capillary number). IP is implemented on a pore network of given connectivity, with each pore assigned a probability of invasion. A boundary surface is formed by filling selected pores with the invading phase, typically on an edge of a rectangular network, or a disk at the center. All pores connected to the boundary surface are available for invasion; the one with the highest assigned probability of invasion is found and invaded. This pore filling modifies the list of pores available for invasion, which is sorted again to find the next pore with the highest assigned probability of invasion, and so on. If the defender phase is incompressible, then pores that become surrounded by the invader (entrapped) are removed from the list. Conversely, entrapped pores are not removed if in the timescale for invader phase advance, the defender fluid is compressible, can escape via film flow (wetting fluid), or will dissolve in the invading phase. Invasion is stopped either when no pores are found that are above a specified cutoff in assigned invasion probability, or when growth has reached a specified spatial extent such as edges of the network (e.g., breakthrough).

IP has been shown to conform reasonably well to the invasion of a random, spatially uncorrelated, two-dimensional pore network by a nonwetting fluid. Under these conditions, the fluid-fluid interface exhibits structure on all scales down to the pore scale and has been measured as fractal [Lenormand and Zarcone, 1985]. However, wetting fluids invading porous networks show much smoother and more macroscopic fluid-fluid interfaces [Lenormand and Zarcone, 1984]. In addition, when a denser/lighter fluid displaces another from above/below in a porous media, gravity/buoyancy-driven fingering occurs under a variety of conditions of low flow (see review by Glass and Nicholl [1996]). These fingers are found to be macroscopic under wetting invasion [e.g., Glass *et al.*, 1989] and microscopic under nonwetting invasion [e.g., Schwille, 1988].

IP was modified by Meakin *et al.* [1992] to include gravity for nonwetting invasion and additionally by Glass and Yarrington [1989, 1996] to include both gravity and the interfacial smoothing mechanism provided by multiple-adjacent-neck-pore-filling facilitation for wetting invasion. These modified forms of IP (MIP) are able to capture the essence of the wetting and nonwetting fluid advancement in porous media where non-pore-spanning communication processes are negligible. For horizontal wetting invasion, macroscopic fronts are simulated, their complication being a function of pore size distribution. For horizontal nonwetting invasion the IP model is maintained, fronts do not form, and the invasion structure is not influenced by the pore size distribution, only by its hierarchy. With gravity, macroscopic gravity-driven fingers are simulated for wetting invasion while pore scale fingers are calculated for nonwetting invasion (again, predicted from simple inclusion of gravity in IP). Nonwetting gravity destabilized invasion has been subsequently studied by Deng *et al.* [1998]. Other forms of MIP have been proposed to accommodate a variety of additional processes, including gas diffusion during drying [Prat, 1993]; film flow, snap-off, and pore-filling facilitation during wetting [Blunt and Scher, 1995]; and viscous forces [Ewing and Berkowitz, 1998]. Upscaled formulations of MIP have been used to model phase displacements such as dense non-aqueous phase liquid (DNAPL) migration within heteroge-

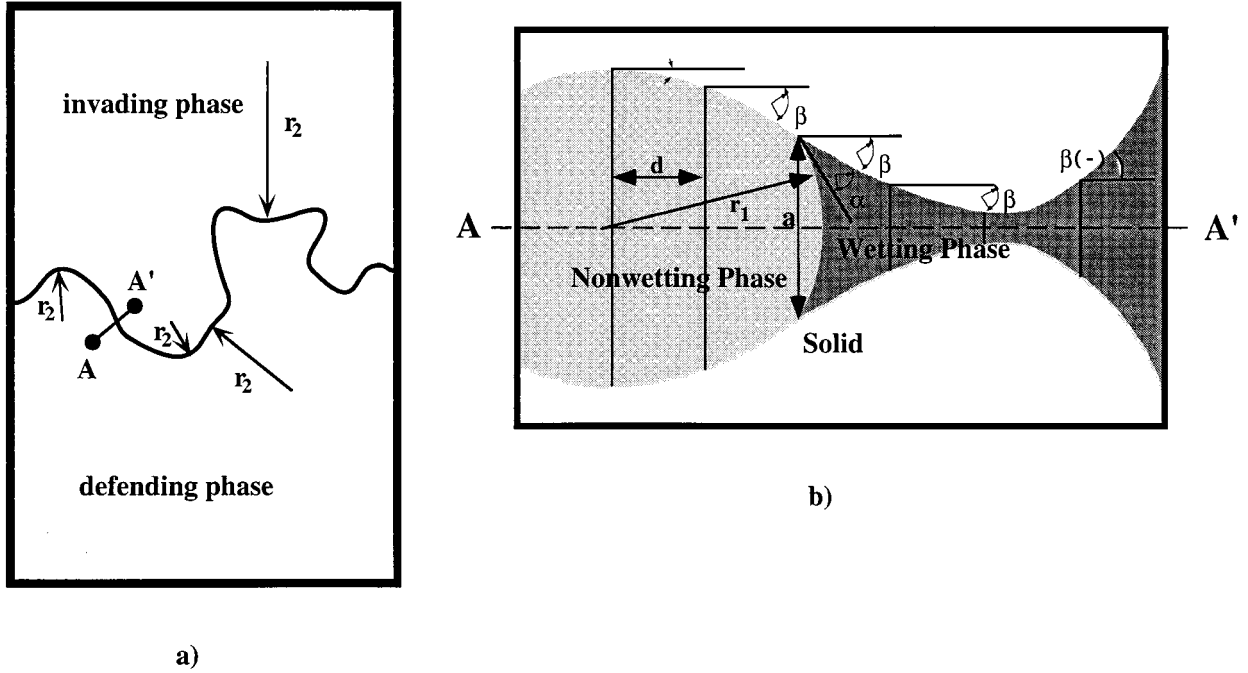


Figure 1. Definition of r_1 and r_2 . (a) Fluid-fluid interface within a fracture as seen looking down on the fracture plane. Local in-plane curvature r_2 is shown at four different locations along the interface between the invading and defending phase. Note that both sign and magnitude of r_2 will vary. (b) A local fluid-fluid interface (along the transect A–A' in Figure 1a) as seen perpendicular to the fracture plane. Fracture (and hence fluid) geometry are conceptualized as being symmetric about a central plane (dashed line). The contact angle (α), convergence/divergence angle (β), and r_1 are defined in this plane; vertical lines illustrate discretization of the aperture field (a) with a grid spacing of d .

neous aquifers [Glass *et al.*, 1995a], and fluid migration under gravity-stabilized situations [Ioannidis *et al.*, 1996].

In the following, we develop a MIP model for low-capillary number (negligible viscous forces or quasi-static) immiscible fluid displacements in horizontal, rough-walled fractures where non-aperture-spanning communication processes within the fracture plane are slow with respect to aperture-spanning fluid displacements. We focus on the interplay between the two radii of curvature that define the local aperture filling pressure along the fluid-fluid interface within the fracture. We conceptualize the fracture aperture field as a planar checkerboard of individual aperture elements (sites) with a fourfold connectivity; the center of each site has a known local aperture. The site invasion pressure (P_c) is a function of the two principal radii of interfacial curvature (r_1 and r_2) and the surface tension (σ) as given by the Laplace-Young relation:

$$P_c = -\sigma \left(\frac{1}{r_1} + \frac{1}{r_2} \right) \quad (1)$$

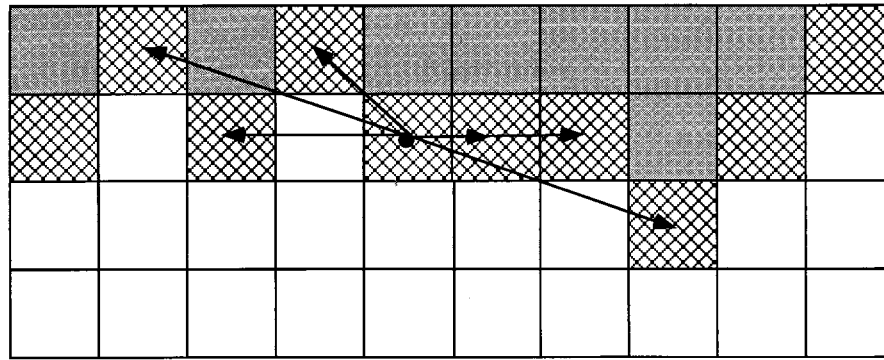
As shown in Figure 1a, we take one principal radius of curvature (r_1) to be normal to the plane of the fracture and the other (r_2) to be in the plane of the fracture. The curvature defined by r_1 will intersect the fracture walls, while that defined by r_2 will not; therefore wettability affects only r_1 . If we assume that the fracture surfaces are symmetric about a mean plane (Figure 1b), r_1 is related geometrically to the local aperture (a) and local convergence/divergence angle of the fracture surfaces (β) through the local contact angle (α) of the fluid-fluid-fracture system:

$$r_1 = \frac{a}{2 \cos(\alpha + \beta)} \quad (2)$$

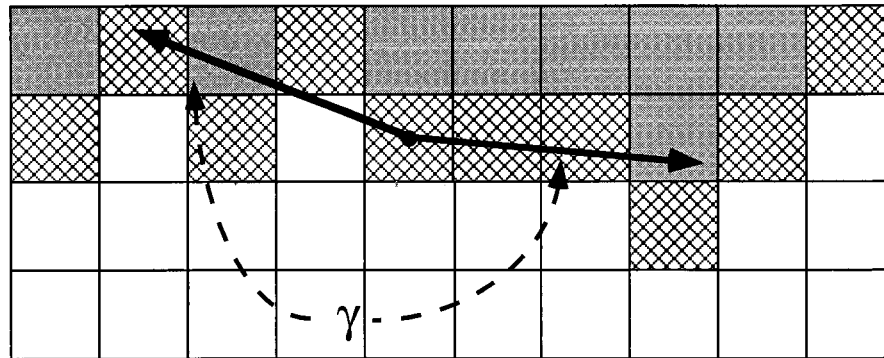
Wettable surfaces are given by $0 < \alpha < 90$ and nonwettable surfaces by $90 < \alpha < 180$. In order to account for spatial variation in surface chemistry and transient or dynamic contact angle [e.g., Dussan, 1979; de Gennes, 1985], α must be considered a function of space and time; β is defined as positive for widening aperture (negative for narrowing), and hence will vary depending on the invasion direction. Note that β has an increasing influence on the invasion process as α approaches 90 from either direction; away from neutral wettability ($\alpha = 90$), the influence of β diminishes.

Along the lines of Glass and Yarrington [1989, 1996], Glass [1993] approximated the effect of r_2 by considering three potential local configurations as defined by the number of adjacent sites filled with the invading fluid. For one adjacent filled site, invasion yields a final local r_2 that is negative and approximately equal to the distance between aperture locations. For two and three adjacent filled sites, the local interface will be much flatter after invasion, and thus r_2 was considered to add a negligible influence (i.e., r_2 is large). This local approach provided reasonable qualitative (i.e., macroscopic invasion fronts) and quantitative (i.e., gravity-driven finger widths) results but overly emphasized the local curvature, yielding grid-dominated, blocky fronts atypical of the experimental data.

Experimental observations show that as the front moves into a new aperture location, it also moves partially into apertures on either side, decreasing the local curvature. In addition,



a) vectors from invasion site to other sites on the interface



b) resultant average vectors that estimate the local interface with included angle γ

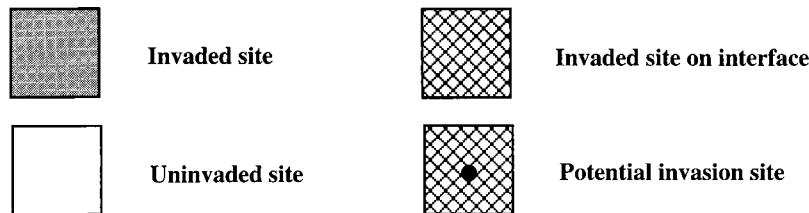


Figure 2. Estimation of r_2 at a potential invasion site. Looking downward onto a checkerboard variable aperture field, blocks (sites) shown in gray are filled with the invading fluid, hatched gray are invaded sites on the active interface, and white are filled with the defender fluid; the hatched white block is the example site for which an invasion pressure including r_2 is calculated. (a) The vectors from the potential invasion site to sites up to three positions away both to the right and to the left along the interface. (b) A weighted average of unit vectors to the right and to the left of the potential invasion site defines the local average fluid interface, and the angle γ used for the calculation of r_2 . Positions used for this calculation should be within a distance λ on each side of the potential invasion site.

regardless of grid resolution, the discretization of a continuous fluid-fluid interface yields many local discontinuities (steps) that are numerically indistinguishable from large local in-plane curvatures. These observations imply that calculation of r_2 must include information from further away than the adjacent site. Here we implement a simple and flexible model for estimating r_2 that both avoids local discontinuities and incorporates information from a selected number of nearby sites along the interface.

Consider r_2 as a function of the angle (γ) between two vectors representing the average interface once a site is invaded (see Figure 2). Noting that r_2 should become infinite or zero when γ approaches 180° or 0° , respectively, we model r_2 as

$$r_2 = \langle r_2 \rangle \tan\left(\frac{\gamma}{2}\right) \quad (3)$$

where $\langle r_2 \rangle$ is a representative r_2 specific to the aperture field under study. To avoid dependence on the discretization resolution of the aperture field (such as that used by Glass *et al.* [1997]), we link the calculation of γ and $\langle r_2 \rangle$ to the spatial structure of the aperture field. We assume the aperture field to be spatially correlated over a length (λ), which we then take as a characteristic length scale. In such a field we expect features defined wholly by in-plane curvature to have approximate diameters of λ and take $\langle r_2 \rangle \sim 0.5 \lambda$. (Note that in analyzing our experimental data, we find the representative curvatures

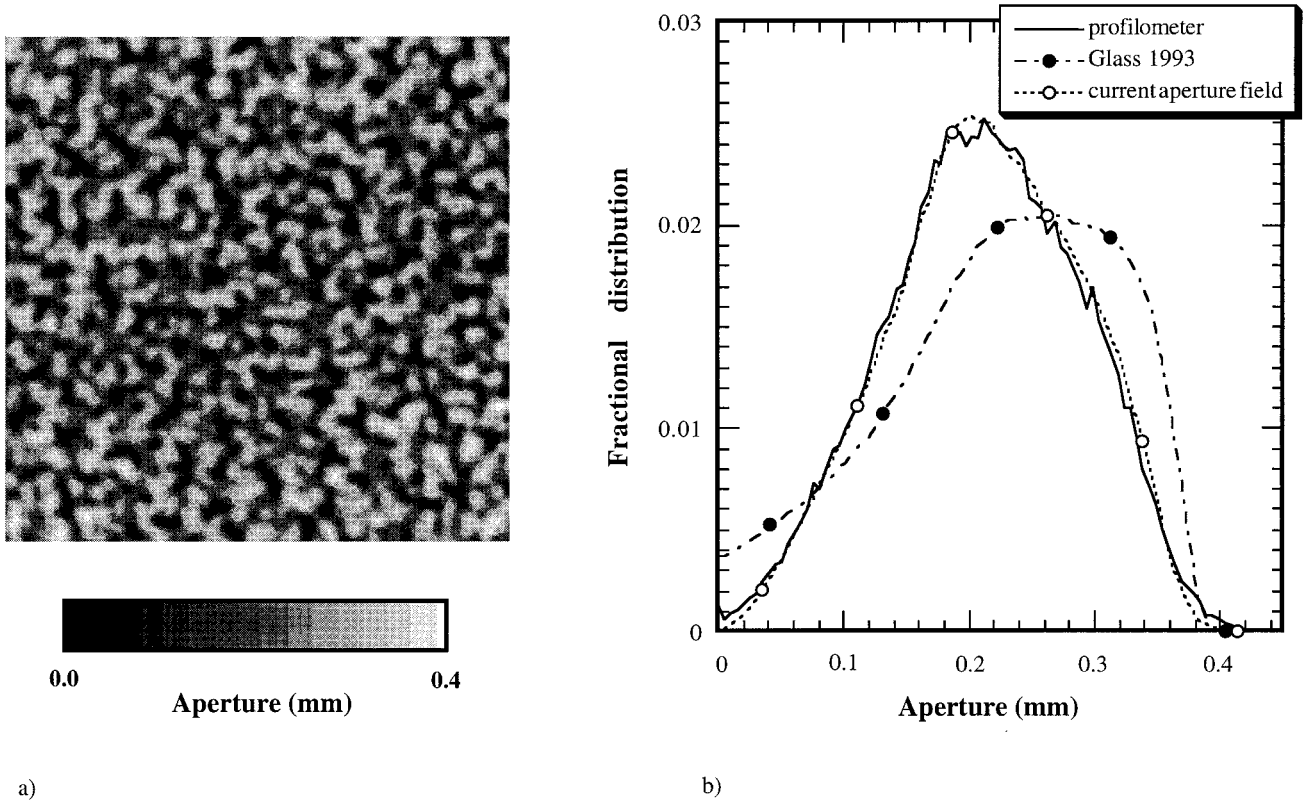


Figure 3. Aperture field used for simulations. (a) A 256×256 pixel (38.4×38.4 mm) segment of the 850×1950 (127.5×292.5 mm) aperture field measured with transmitted light imaging by *Nicholl and Glass* [1994]. (b) Normalized histogram of the aperture field used in our simulations compared to that used by *Glass* [1993] and modeled from surface measurements over a small area taken with a laser profilometer.

where growth occurs to have this value as an upper limit.) The vectors defining γ (right or left; see Figure 2) are determined as a weighted average of unit vectors extending from the potential invasion site to each neighboring site along the interface within a distance λ (right or left). The weighting factor for each unit vector is calculated as the reciprocal of the neighbor number (1 for nearest, 2 for next nearest, etc.) raised to a power.

Substituting for r_1 and r_2 in (1) yields

$$P_c = \sigma \left(-\frac{2 \cos(\alpha + \beta)}{a} + \frac{2}{\lambda \tan(\gamma/2)} \right) \quad (4)$$

As invasion proceeds, values of P_c at each site are used to determine invasion order; the lower the P_c , the higher the probability of invasion. Numerical implementation of MIP requires several modifications to the IP invasion sequence described previously. After a site fills with the invading fluid, the r_2 component of P_c (second term in parentheses of (4)) is recalculated for all neighboring sites along the active interface within the distance λ . Then, for nearest neighbors of the invaded site, β must be recalculated for the new local invasion directions. The β that yields the most negative r_1 component (first term in parentheses of (4)) for wetting and smallest positive for nonwetting is used in the recalculation of P_c . Finally, if we tie the invaded volume to a flow rate, then time is imposed on the invasion process, and dynamic contact angle may be explicitly considered. We emphasize that the current model for r_2 is approximate, and requires aperture field discretization smaller than λ ; formulation of precise rules for

optimal discretization requires additional study and will not be addressed further here.

3. Simulation Design for Relative Importance of r_1 and r_2

A full study of (4) requires exploring parameter space for both aperture (a) and contact angle (α) as random variables, each characterized by their mean, variance, and spatial correlation lengths; additionally, α must be considered as a function of time. As a first step toward understanding the control of local interfacial geometry on phase invasion structure, we restrict α to be constant in time and space. We also choose to further simplify (4) by neglecting the influence of β , which will be weak for α away from 90° . With these simplifications, (4) can be nondimensionalized to yield

$$P_c^* = -\frac{\text{sign}(\cos \alpha)}{r_1^*} + C \frac{1}{r_2^*} \quad (5)$$

with

$$P_c^* = \frac{\langle a \rangle}{2\sigma |\cos \alpha|} P_c \quad r_1^* = \frac{a}{\langle a \rangle} \quad r_2^* = \tan\left(\frac{\gamma}{2}\right)$$

$$C = \frac{\langle a \rangle}{\lambda |\cos \alpha|}$$

where $\langle a \rangle$ is the mean aperture, and C we define as a dimensionless curvature number that on average weighs the relative

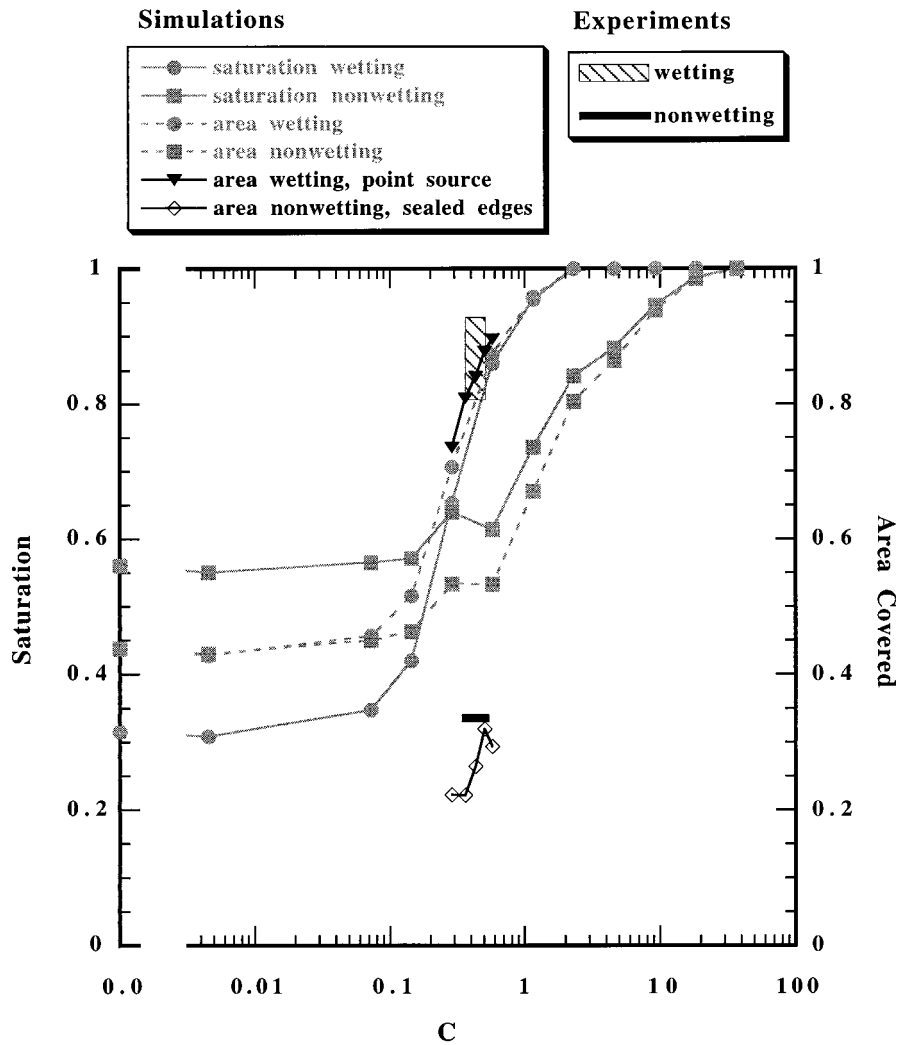


Figure 4. Fracture saturation (volume and area) as a function of C . Volumetric and areal invading phase saturations were measured at fracture saturation for both wetting and nonwetting cases. For both wetting and nonwetting cases, volumetric and areal saturations are seen to converge and approach 1 (full saturation) as C increases. The experiments used for comparison purposes allow only measurement of areal saturation. Experimental measurements during wetting invasion from a point source (hatched box) coincide very well with a limited suite of simulations corresponding to experimental values (solid triangles). The nonwetting experiment (short dark line) was run with closed side boundary conditions and stopped short of saturation (breakthrough); the large entrapped regions resulting from this boundary (see Figure 12) acted to reduce fracture saturation. A limited suite of simulations corresponding to experimental values of C were run to breakthrough under these boundary conditions (open diamonds); results correspond very well with the experimental observations.

magnitude of the r_1^* and r_2^* terms. The sign of r_1 is retained to distinguish between wetting and nonwetting invasion in the r_1^* term. The field of r_1^* values is determined by aperture geometry, while the distribution of r_1^* that is actually invaded and r_2^* are path-dependent variables coupled through C in a highly nonlinear manner.

We see from (5) that the phase growth behavior of a given fracture with random aperture field of correlation length λ is determined simply by its dimensionless distribution r_1^* and the curvature number C . For a given r_1^* distribution a single value of C represents a family of geometrically scaled similar fractures (defined value of $\langle a \rangle / \lambda$) within a given fluid-fluid-solid system (defined α) or denotes different fluid-fluid-solid systems (different α) with compensating geometries (different $\langle a \rangle / \lambda$). Variation of C embodies varying the geometry ($\langle a \rangle / \lambda$)

for a given fluid-fluid-solid system (α), the fluid-fluid-solid system (α) for a given geometry ($\langle a \rangle / \lambda$), or both.

The range of C for which (5) is valid will be limited; for curvatures to be correctly represented by the model, the aperture must be spanned and r_2 must be wholly determined by local variation in the aperture field. The first constraint limits the maximum value of $\langle a \rangle$, and the second limits the minimum value of λ ; thus $\langle a \rangle / \lambda$, which defines system geometry, likely varies from very small to between ~ 1 and 10. Additionally, (5) is limited with respect to α ; as α approaches 90° from either above or below, the influence of β becomes nonnegligible and (5) will no longer hold. In combination with the geometric constraints, the upper limit of validity for (5) with respect to C is likely to be in the range of ~ 5 to 50 depending on the r_1^* field in question.

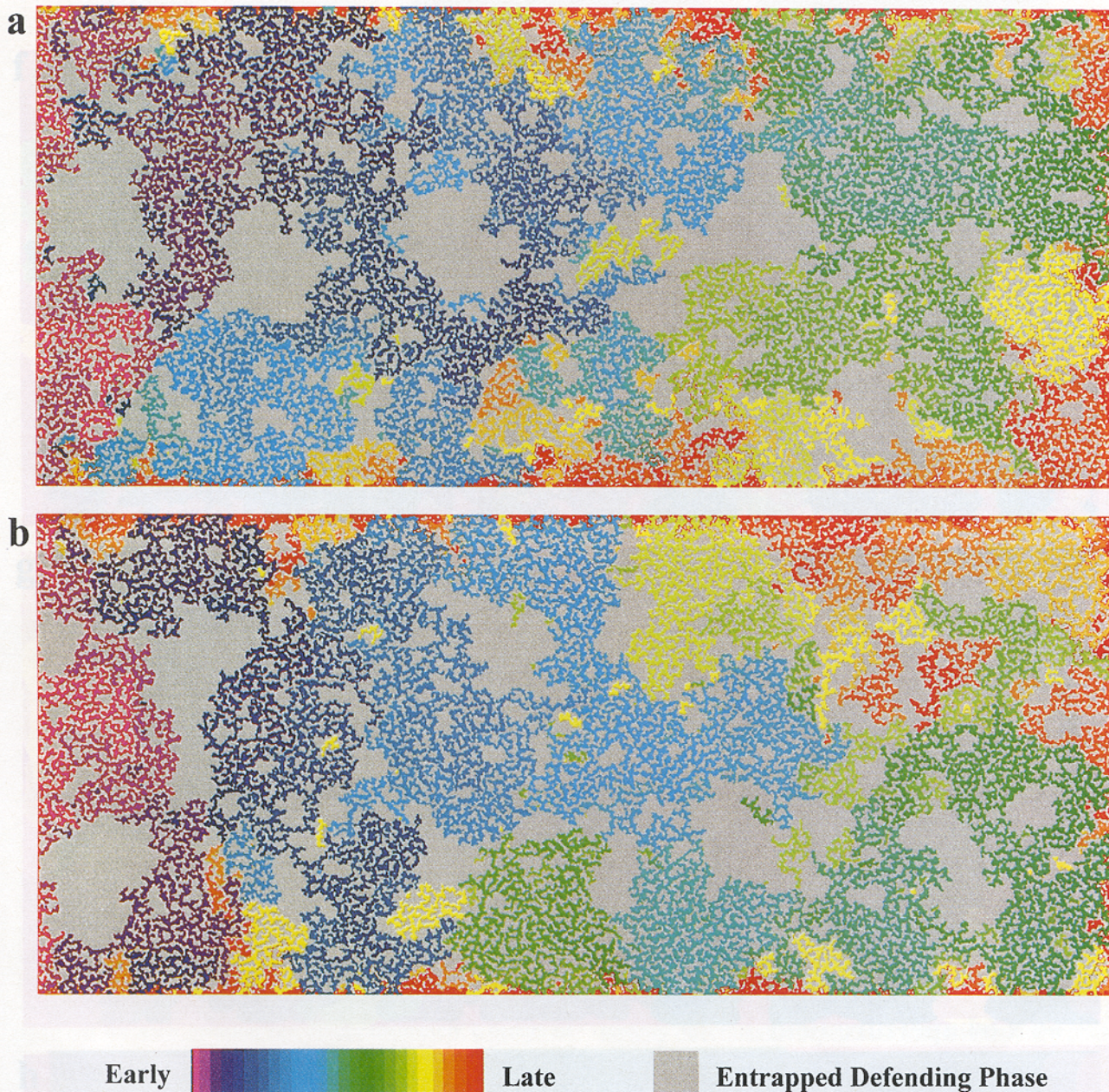
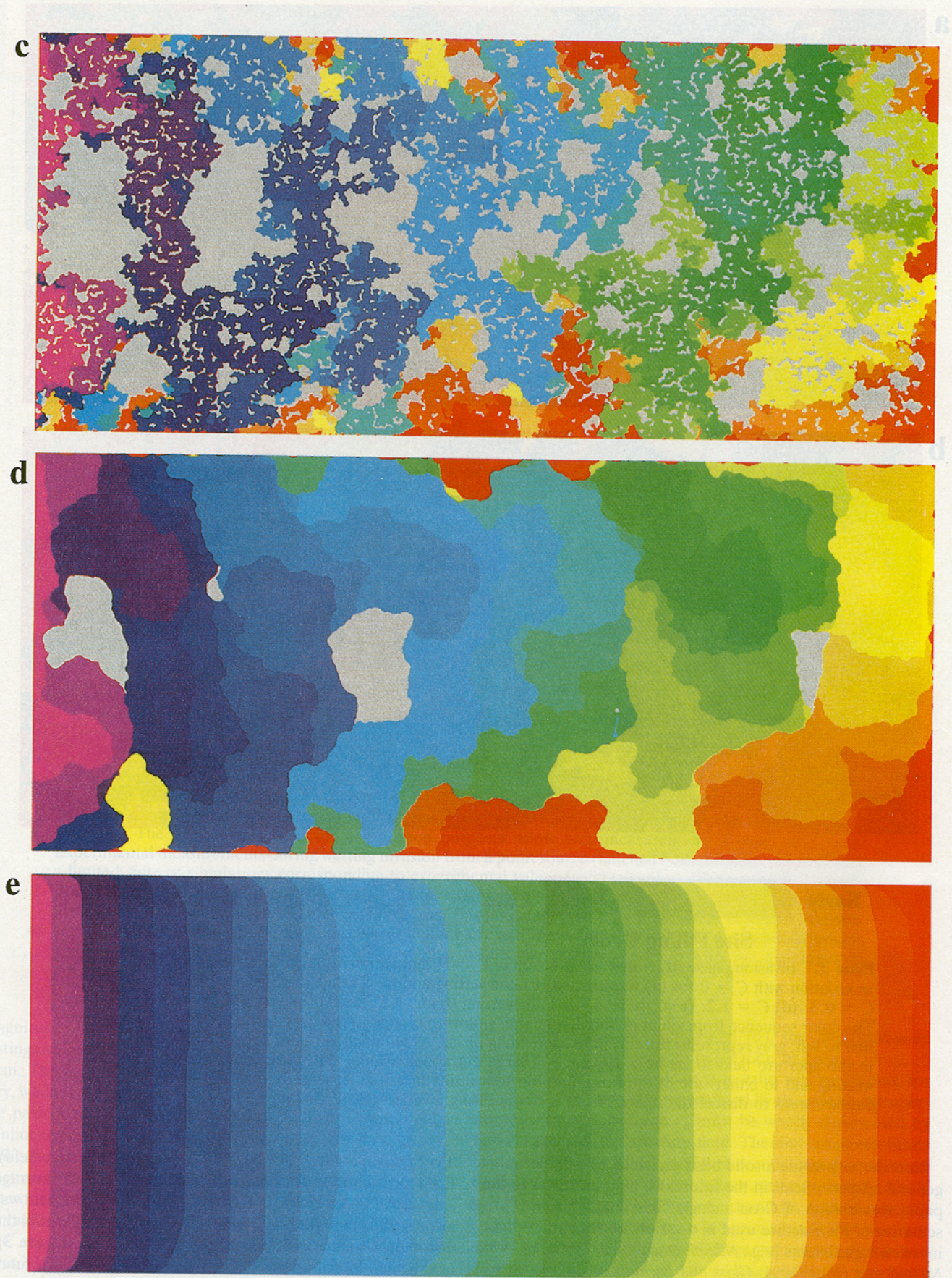


Plate 1. Invasion phase structures as a function of C . MIP simulation of the invasion sequence (left to right) to saturation with $C = 0$ for (a) wetting and (b) nonwetting and for a range of C values for both wetting ((c) $C = 0.3$; (d) $C = 1.2$; (e) $C = 38.5$) and nonwetting ((f) $C = 1.2$; (g) $C = 9.6$; (h) $C = 38.5$) invasion. The color sequence from violet to blue to green to yellow to orange to red depicts the order of invasion from first to last; gray represents the entrapped defending phase. Note the influence of large-scale features ($\sim 50 \lambda$) in the aperture field to create a sequence of large entrapped regions down the centerline of the field for wetting and to either side of the centerline for nonwetting invasion. At large C note the influence of small contact areas to dissect the smooth front for nonwetting invasion (Plate 1h).

In order to provide a solid basis on which to consider more general aperture fields in the future, we limit ourselves in this paper to variation of C on a single “baseline” r_1^* field representative of the fracture used in a variety of our earlier phase invasion experiments [e.g., Nicholl *et al.*, 1992, 1993a, b, 1994; Nicholl and Glass, 1994; Glass and Nicholl, 1995a, b]. An aperture field for this fracture was measured by Nicholl and Glass [1994] with a CCD camera-based light absorption technique yielding the field as a regular grid of 850×1950 square pixels

0.143 mm on a side (127.5×292.5 mm fracture aperture field). Each measurement at a pixel represents a “pixel area” average aperture at that location in the field. The mean of the field was measured to be 0.215 mm, and analysis of the field yields the distribution’s standard deviation of 0.075 mm (see Figure 3). Location-to-location variance of the aperture field as a function of separation length was measured on both primary axes and on the principal diagonals, yielding an isotropic spatial correlation length, λ , of approximately five pixels (~ 0.72 mm).



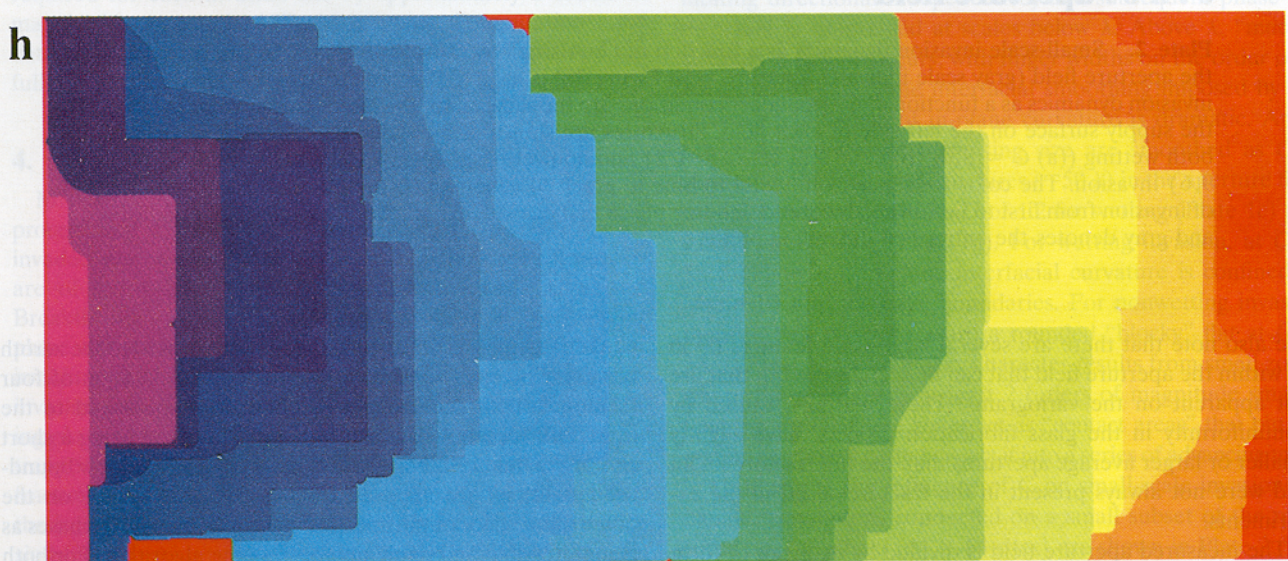
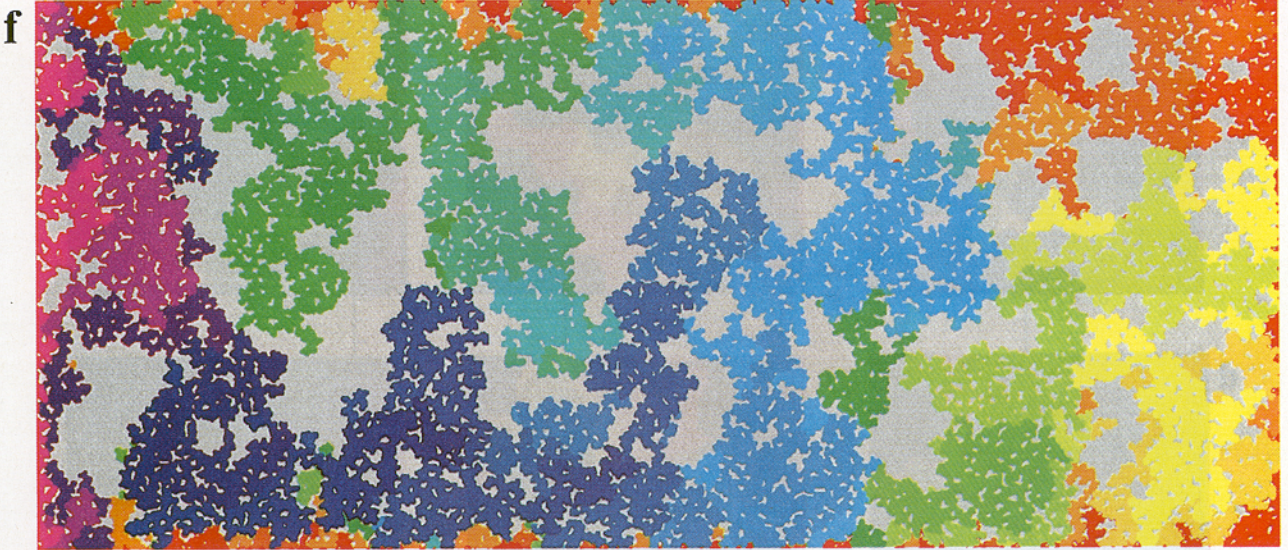
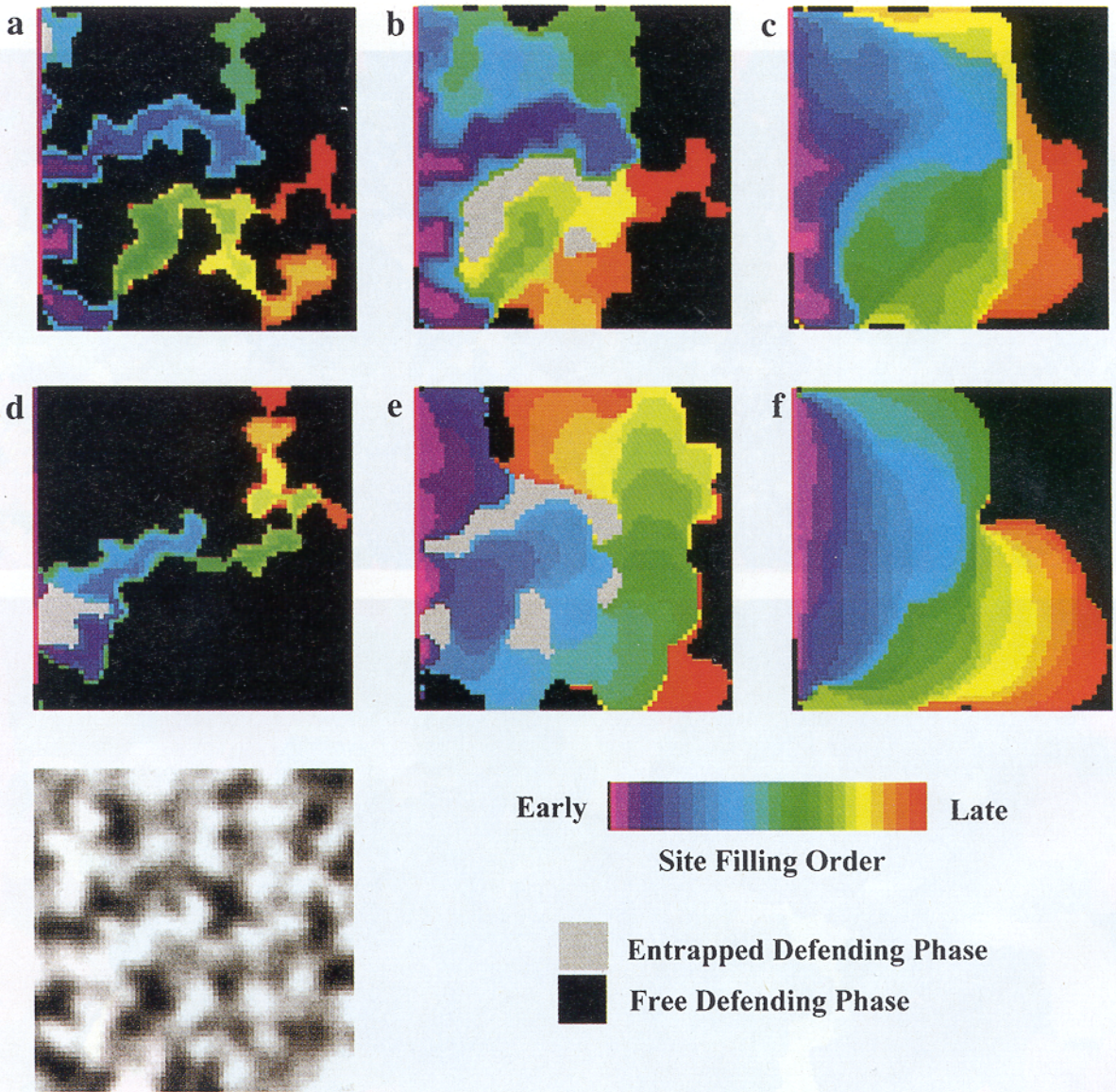


Plate 1. (continued)



64 x 64 aperture field

Plate 2. Small-scale invasion dynamics as a function of C . A small 64×64 pixel (9.6×9.6 mm) region of the aperture field (gray scale indicates aperture as in Figure 3a) is used to illustrate the small-scale details of invasion dynamics as a function of C . Boundary conditions are the same as for the large-scale simulations, with the supply surface on the left side of each field. Structures are shown at breakthrough from left to right for both wetting ((a) $C = 0.0$; (b) $C = 0.3$; (c) $C = 1.2$) and nonwetting ((d) $C = 0.0$; (e) $C = 1.2$; (f) $C = 9.6$) invasion. The color sequence from violet to blue to green to yellow to orange to red depicts the order of invasion from first to last, black denotes defending phase that can still exit the field through the boundaries, and gray denotes the entrapped defending phase.

We also note that there are several large-scale features ($\sim 50 \lambda$) within the aperture field that can be seen by eye but that are not apparent on the variograms. These features, caused by nonuniformity in the glass fabrication process, have slightly smaller or larger average apertures than the full fracture mean and were not always present in the fractures used in the experiments.

The measured aperture field is divided by its mean to form a checkerboard r_1^* field with sites (or elements) at each of the measured locations. Our discretization contains five sites per correlation length; for calculation of γ we weight the vectors

equally (reciprocal of the neighbor number raised to the zeroth power). The sites are networked with a coordination of four (square lattice) such that each element is connected to the right, left, top, and bottom. Invasion is initiated along a short axis of the field by filling the first row of sites. Free-flow boundary conditions are imposed for the defending phase on the other three edges of the aperture field. We treat both phases as incompressible and implement a trapping algorithm. For both wetting and nonwetting invasions we conduct simulations on the full 850×1950 site aperture field for C over its full range of influence with values covering roughly 3 orders of magni-

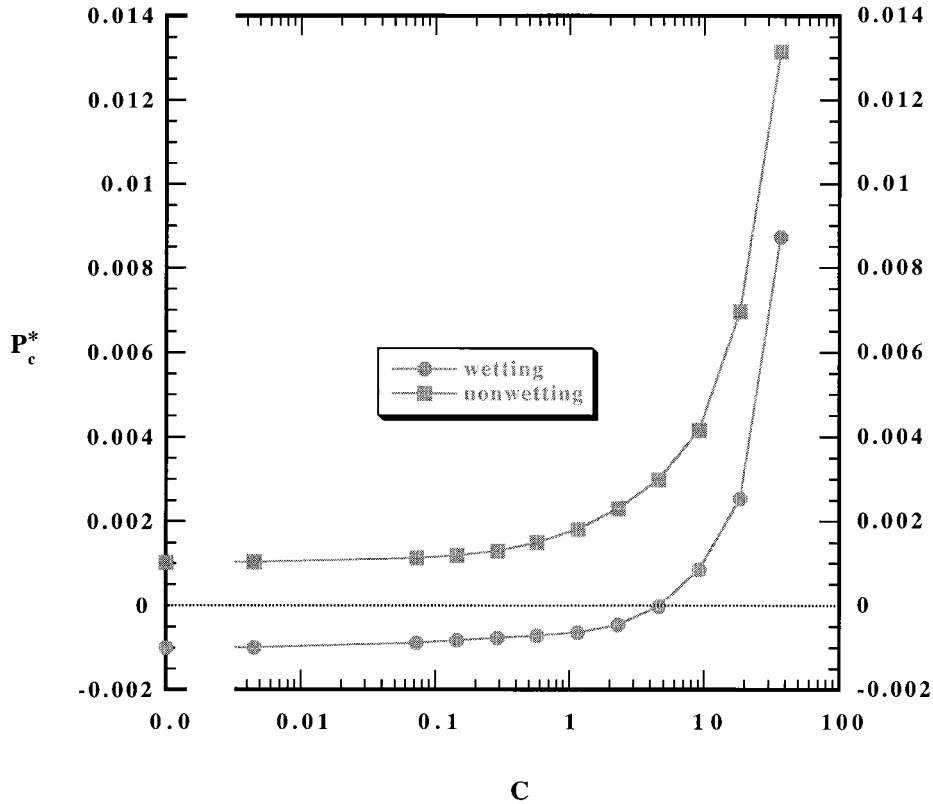


Figure 5. P_c^* as a function of C . The dimensionless pressure required to span the fracture (breakthrough) is found to increase slowly with C for both wetting and nonwetting invasion until $C \sim 1$, after which it increases rapidly. Increasing C above ~ 5 renders the fracture effectively hydrophobic even for hydrophilic fracture surfaces.

tude (4.7×10^{-2} to 3.85×10^1) and additionally for C of zero (IP results). As stated above, this variation in C can be interpreted as variation of $\langle a \rangle / \lambda$, or α for the field within the discussed limits. For α of 0 or 180, C for our baseline fracture determined by geometry ($\langle a \rangle / \lambda$) is ~ 0.3 . Our treatment of interfacial curvature increases the number of computations required for each invasion site by approximately 2 orders of magnitude over standard IP with trapping. Computational and data storage requirements for implementation of MIP on the full 1950×850 measured aperture field are significant.

4. Simulation Results and Analysis

MIP simulation yields a step-by-step history of the invasion process that includes the pressure required to occupy each invaded site on the lattice. Two steps in the invasion process are of particular interest, “breakthrough” and “satiation.” Breakthrough is defined as the first contact of the invading phase with the downstream boundary of the aperture field (i.e., invading phase spans the long axis). Following breakthrough, invasion is continued until all sites are filled with either invading phase or trapped defending phase. Because invasion of the trapped defending phase is not allowed in our simulations, fracture saturation does not increase beyond this point; hence the fracture is satiated. Plates 1a and 1b show sequential invasion (color) and satiated structures on the 1950×850 grid for $C = 0$ for wetting and nonwetting invasion, and Plates 1c–1h show C values of 0.3, 1.2, and 38.5 for wetting invasion and 1.2, 9.6, and 38.5 for nonwetting invasion. Intermediate C values

for Plates 1c, 1d, 1f, and 1g were chosen such that the number of sites occupied by the invading phase was similar for both wetting and nonwetting cases.

IP with trapping ($C = 0.0$) allows for two possible phase structures, one each for wetting and nonwetting invasion (see Plates 1a and 1b, respectively). For IP, capillary fingering (exhibiting directional independence) and subsequent phase entrapment is suppressed at scales below λ . Above λ , “macro” capillary fingering occurs, with finger widths on the order of λ . As seen in Plate 1, the interfacial smoothing imposed by the increasing influence of in-plane curvature is dramatic. Aperture field features of increasing size are smoothed as C is increased; the large-scale features ($\sim 50 \lambda$) in the aperture field are seen to persist up to a C of 1.2 for wetting (Plate 1c) and 9.6 for nonwetting (Plate 1g). For wetting invasion, at $C = 38.5$ (Plate 1e), in-plane interfacial curvature is confined to within 10λ of the edge boundaries. For nonwetting invasion the interface evolves toward a rounded “blocky” flat at $C = 38.5$ (Plate 1h). The blocky character results from small zones where the aperture is at least 2 orders of magnitude smaller than the mean. These zones act as “contact areas” that pin the nonwetting interface and dissect it into a series of advancing units.

To illustrate the influence of C on small-scale invasion dynamics, simulations conducted on a small subset of the measured aperture field (64×64 sites) are shown in Plate 2. The aperture field consists of small rounded regions or “basins” of correlated large or small apertures of order λ wide. We see that for IP ($C = 0$), the invading fluid tends to fill up a basin

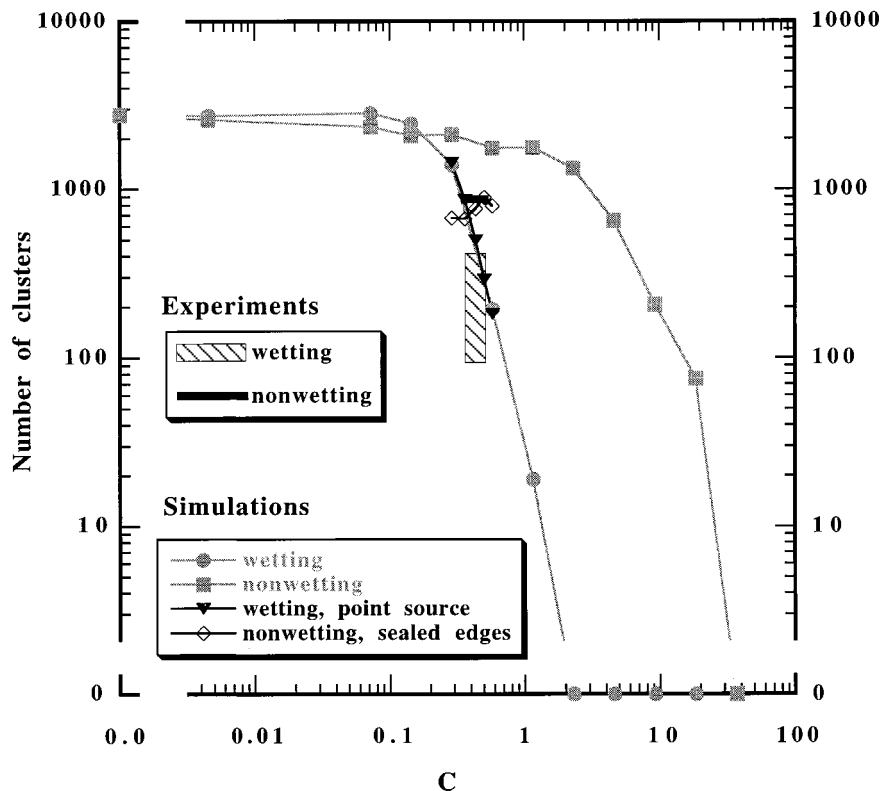


Figure 6. Number of entrapped defending phase clusters as a function of C . The total number of defending phase clusters trapped at fracture saturation is seen to decrease with C for both wetting and nonwetting cases. Experimental measurements for wetting invasion (hatched box) agree well with simulations (solid triangles). Simulations of nonwetting invasion run to breakthrough under closed side boundary conditions (open diamonds) coincide almost exactly with the nonwetting experimental observations (short dark line).

before spilling over the surrounding basin “edge” (see Plates 2a and 2d). On close inspection, the spillover of the basin edge often occurs at a single site from which a narrow tendril grows to the center of the next aperture basin. Outward expansion then fills the new basin from its center. As a result of these invasion dynamics, entrapment of the defending fluid tends to occur at, or above λ . Introduction of in-plane curvature significantly alters invasion dynamics. As C increases, development of the invasion front becomes macroscopic; the edge spillover, tendril formation, and basin fill-up dynamics are gradually suppressed (see Plates 2b, 2c, 2e, and 2f). Macroscopic capillary fingers gradually increase in width with C until reaching the width of the system; that is, the structure of the invading phase becomes more compact and occupies a larger fraction of the fracture plane.

4.1. Quantitative Analysis of Phase Structures (Breakthrough and Final)

Fractional occupancy of the grid by the invading phase is considered for both areal and volumetric measures. Areal saturation is defined as the fraction of sites that are occupied by the invading phase. Volumetric saturation is defined as the fraction of the total fracture volume that is occupied by the invading phase, as calculated by summing the local aperture volume of the invaded sites. Invading phase saturations (areal and volumetric) measured at fracture saturation are shown to increase as a function of C from minimums at the IP limit to full saturation (1.0) (see Figure 4). Areal saturation at the IP

limit ($C = 0.0$) is essentially identical for wetting and nonwetting invasion (~ 0.44), suggesting that in this aperture field, the spatial correlation of small apertures is nearly identical to that of large apertures (also compare Plates 2a and 2d, where the structure of the capillary fingers are seen to be near identical).

At small C , volumetric saturation for nonwetting phase invasion exceeds the areal saturation, while the converse is true for wetting invasion. This observation reflects the differing phase occupancies within the aperture field for wetting and nonwetting invasion. In the absence of in-plane curvature ($C = 0.0$), wetting invasion preferentially occupies the small apertures, and nonwetting invasion the large apertures. Where in-plane curvature dominates (large C), the macroscopic nature of the invasion front causes the distribution of apertures filled to closely resemble the aperture distribution; hence the differences between volumetric and areal saturation become negligible. Measurements of areal and volumetric saturation of the invading phase taken at breakthrough exhibit behavior similar to that shown in Figure 4 with necessarily reduced values of saturation (not shown).

Invading phase saturations are positively correlated with C (Figure 4); however, the increase with C starts sooner for wetting invasion than for nonwetting. This occurs because of the nonlinear interaction between C and chosen r_1^* . Increasing C changes the distribution of apertures invaded to include larger apertures for wetting invasion and smaller apertures for nonwetting invasion. The first term in (5) is inversely propor-

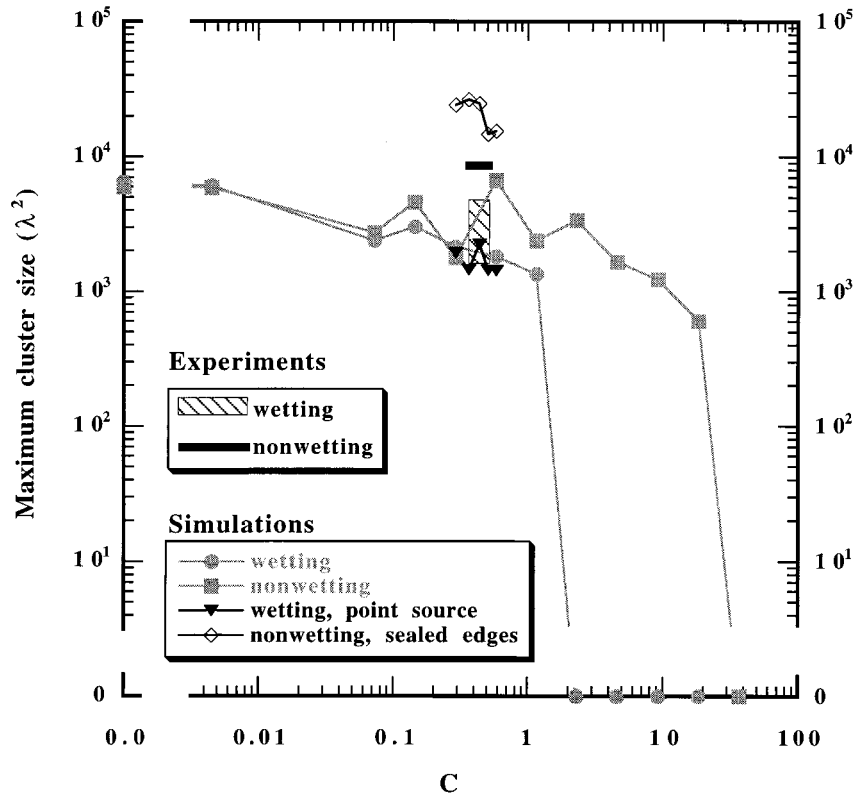


Figure 7. Largest cluster of entrapped defending fluid as a function of C . Area of the largest entrapped defending phase cluster at fracture saturation is measured in units of aperture field correlation length (λ^2). Measurements decrease slowly with C and then abruptly drop from macroscopic to zero. Experimental measurements for wetting invasion (hatched box) coincide closely with the simulations (solid triangles). Simulations of nonwetting invasion run to breakthrough under closed side boundary conditions (open diamonds) produced a larger entrapped region than was observed experimentally (short dark line).

tional to r_1^* ; therefore, as C increases, the magnitude of this term will on average decrease for wetting invasion and increase for nonwetting invasion.

The influence of C on the invading structure is also seen in the dimensionless threshold pressure required to span the fracture (breakthrough, Figure 5). The threshold P_c^* increases slowly up to $C \sim 1$, after which it rapidly rises. Inclusion of in-plane curvature yields an “effective hydrophobic” response for hydrophilic surfaces ($\alpha = 0.0$) when C is above ~ 5 . It is unclear whether this effect is real or simply an artifact of the in-plane curvature model for large C .

Increasing the importance of in-plane curvature causes both the total number of entrapped clusters and the size of the largest cluster to decline (see Figures 6 and 7, respectively). For both wetting and nonwetting cases the total number of entrapped clusters decreases slowly with increasing C and then suddenly falls to zero; the nonwetting curve is shifted significantly to the right (larger C) of the wetting curve (Figure 6). Over the same range of C , the size of the largest entrapped cluster size decreases more rapidly than the total number of entrapped clusters (Figure 7). At C above ~ 1.0 the largest cluster trapped by wetting invasion rapidly drops to zero; for nonwetting invasion this rapid drop-off occurs at $C \sim 20$, yielding distinct trends for wetting and nonwetting invasion.

The interfacial complication of entrapped phase clusters is also influenced by C . For any given cluster the ratio of perimeter length to area provides a scale-dependent measure of compactness. Because the maximum entrapped cluster size is

also a function of C , we remove scale dependency by comparing the perimeter of the largest entrapped cluster to that of a circle with the same area. Results show that from the highest complication at $C = 0$ (IP) where both wetting and nonwetting cases yield nearly identical results, the entrapped clusters become both smaller (Figure 7) and more compact (Figure 8) as C increases. Once again, we find distinct trends for wetting and nonwetting invasion. We note that measurement of perimeter length on gridded data does introduce inherent inaccuracy, as lines not coincident with the grid are approximated by stair-step features; however, the observed trends will remain. In addition, because pixelated data are square in nature, the measure shown in Figure 8 will have a minimum slightly higher than 1 (~ 1.12).

4.2. Summary

As C is increased, fracture saturation increases, while the complexity of both the invasion front and entrapped structure behind the front decreases. The relatively smooth changes observed in quantitative measures with increasing C indicate that the second term in (5) gradually increases in importance from negligible to dominant. Beyond this obvious and large influence of C on the phase invasion structure, a more subtle behavior is seen in the deviation of the measures for wetting versus nonwetting invasion. All measures change most significantly between C values of 0.1 and ~ 2 for wetting invasion and 1 and ~ 38 for nonwetting invasion. Outside of this zone of variation, the wetting and nonwetting measures converge for

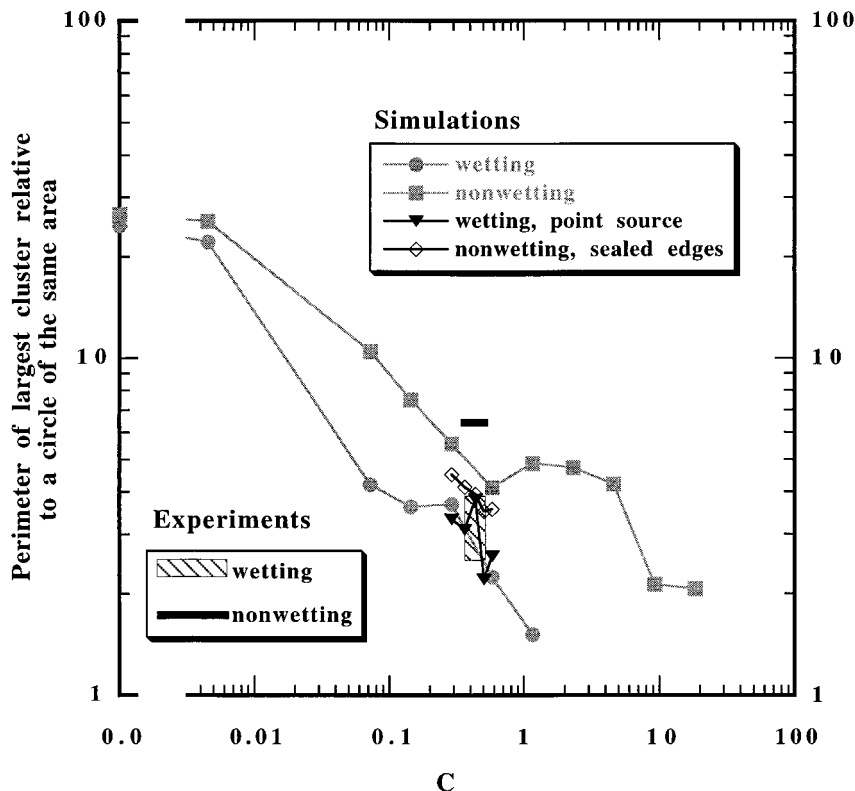


Figure 8. Perimeter of the largest cluster of entrapped defending fluid relative to a circle of equivalent area, shown as a function of C . Compactness of the entrapped clusters was evaluated by normalizing perimeter length of the largest entrapped defending phase cluster with that of a circle of equivalent area. Complication of the cluster perimeter is seen to decrease with C for both wetting and nonwetting cases. Experimental measurements for wetting invasion (hatched box) closely coincide with the simulation results (solid triangles). Simulation of nonwetting invasion run to breakthrough under closed side boundary conditions (open diamonds) trapped larger clusters than were observed in the experiment (see Figure 9); contact between the largest simulated cluster and the side boundary produced a more compact structure than was observed in the experiment (short dark line).

all quantities except volumetric saturation and P_c^* . Since it is apparent that large and small apertures exhibit similar spatial correlation, this response of all measures with respect to C demonstrates an essential difference between wetting and nonwetting invasion within a fracture that is independent of contact angle hysteresis. In general, contact angle hysteresis causes the nonwetting invasion angle to be greater than 180 minus the wetting contact angle, and will therefore act to decrease C with respect to the original wetting value; for a given fracture, contact angle hysteresis will increase the C -induced differential response between wetting and nonwetting invasion for all structural measures.

While the distribution and spatial structure of the possible r_1^* is prescribed for a simulation, the actual distribution of r_1^* chosen during invasion is a function of C and is very different for wetting and nonwetting invasion. With increasing C , the r_1^* -chosen distribution shifts to increasingly resemble that of the aperture field. In the case of wetting invasion this means that larger apertures are preferentially invaded, decreasing the importance of the first term (r_1^*) of (5) and facilitating the dominance of the second term (r_2^*). The converse is true for nonwetting invasion, where increasingly smaller apertures are filled; the first term of (5) increases with decreasing aperture size, opposing the influence of the second, and slows the change of saturation, entrapped cluster number and size, and

overall complexity with C . Therefore, at any given value of C within the range where C has influence but is not dominant, wetting invasion will form less-complicated structures than nonwetting invasion.

Finally, we note that we have considered only one aperture field of limited size ($\sim 170 \times 390 \lambda$); as a result, variation of quantitative measures with C is not completely smooth (Figures 4 and 6–8). A Monte Carlo approach that considers a large number of statistically similar r_1^* fields would be expected to produce smooth curves for the summary statistics. Each simulation set from such a study should yield the same trends as our current study and be a bit rough (such as seen in the current results); however, the combination of all simulations should yield smooth curves with defined variance.

5. Comparison to Experiments

In recent years we have conducted a number of experiments exploring air-water invasion processes in fractures formed from the same material as the one measured and used in the simulations presented above. In our experiments, two pieces of commercially available textured glass (152 mm \times 305 mm) were placed in a transparent test cell such that the two textured surfaces formed an aperture field. The textured glass was smooth below the roughness imposed by the texturing process,

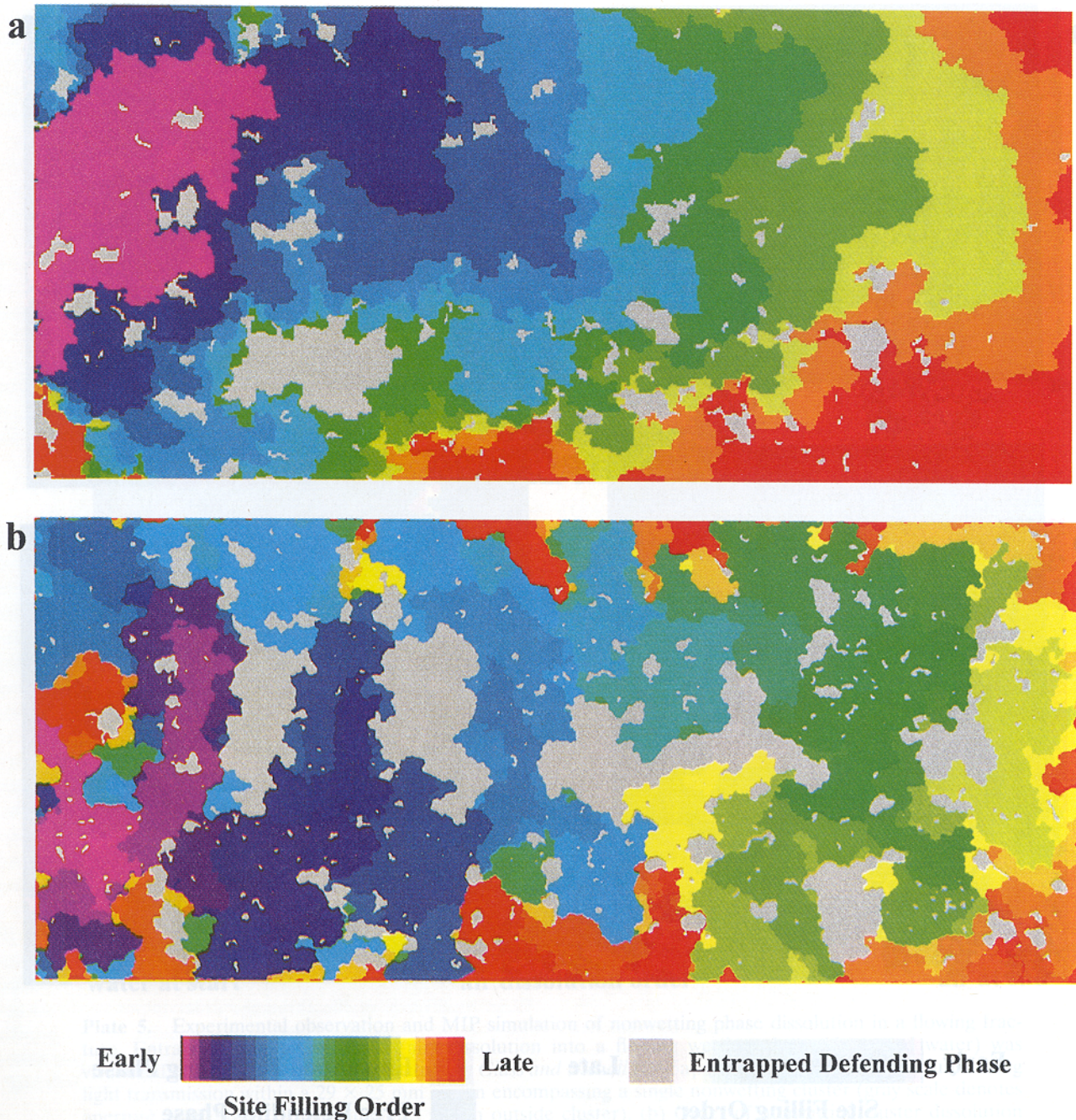


Plate 3. Experimental observation and MIP simulation of horizontal wetting phase invasion. (a) Water is imbibed into the horizontal, air-filled baseline fracture from a point source located at the middle of the left edge. All edges of the fracture were open, allowing air to escape freely. An approximately 116×280 mm section of the 152×305 mm fracture is shown (the gasket which forms the confinement cell obscures part of the image). Flow rate for this experiment (F91) was set at ~ 0.018 mL/min. (b) MIP simulation for flow from a point source at $C = 0.45$ (contact angle of 48°). The color scale from violet to red shows the order of advancement; entrapped phase is shown in gray.

thereby minimizing microroughness-induced film flow of the wetting phase within the fracture. In order to obtain statistically repeatable aperture fields, large-scale variations were minimized by applying a confinement pressure (20 pounds per square inch, or 137,900 Pa) normal to the fracture plane. The transparent sample/test cell was backlit such that phase structure data within the fracture plane could be collected with CCD digital cameras. Contrast between the fluid phases (air,

water) was enhanced by adding dye (FD&C blue #1) to the water. Gaskets forming the confinement cell obscured the outer edges (~ 10 mm) of the fracture plane, so the full fracture could not be viewed. Details of this experimental system are given by Nicholl *et al.* [1992, 1993a, b, 1994], Nicholl and Glass [1994], and Glass and Nicholl [1995a]. After each experiment, the cell was disassembled, the fracture plates were washed with deionized water followed by isopropyl alcohol,

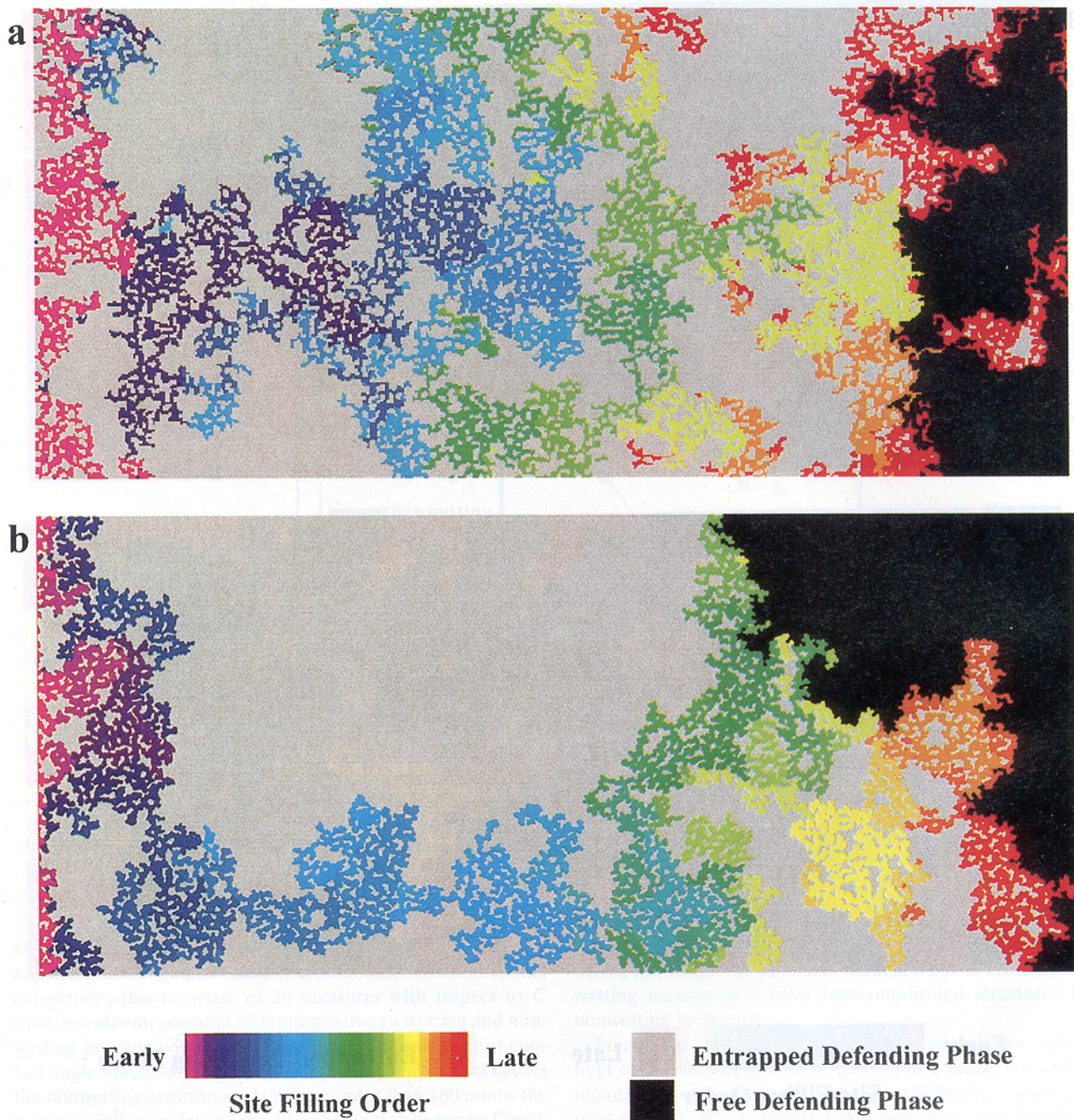


Plate 4. Experimental observation and MIP simulation of horizontal nonwetting phase invasion. (a) The baseline fracture was sealed along the long edges, and flow manifolds were placed across the full width of the upstream (left) and downstream (right) boundaries. After fully saturating the fracture with water, air was supplied slowly to the upstream boundary using a syringe pump, and the downstream boundary was vented to atmospheric pressure. An approximately 116×280 mm section of the 152×305 mm fracture is shown (the gasket which forms the confinement cell obscures part of the image). (b) MIP simulation for closed side boundaries at $C = 0.45$ (contact angle of 48°). The color scale shows the order of advancement from violet (first) to red (breakthrough); entrapped fluid is shown in gray, and free defending fluid is shown in black.

and the cell reassembled. Occasionally, the fracture plates broke and were replaced with pieces cut from the same textured glass stock. Visual inspection of water droplets placed on pieces of new and broken (after retiring) textured glass surfaces showed contact angles to be between 35° and 55° . Because aperture fields used in all experiments were formed from a relatively homogeneous material that was consistently pre-

pared and placed under a repeatable confinement pressure, we expect that these experimental aperture fields were statistically equivalent to the one measured and used for our MIP simulations presented above.

While these past experiments were not specifically designed to test the MIP model, they do provide for preliminary evaluation of model validity. We first consider horizontal phase

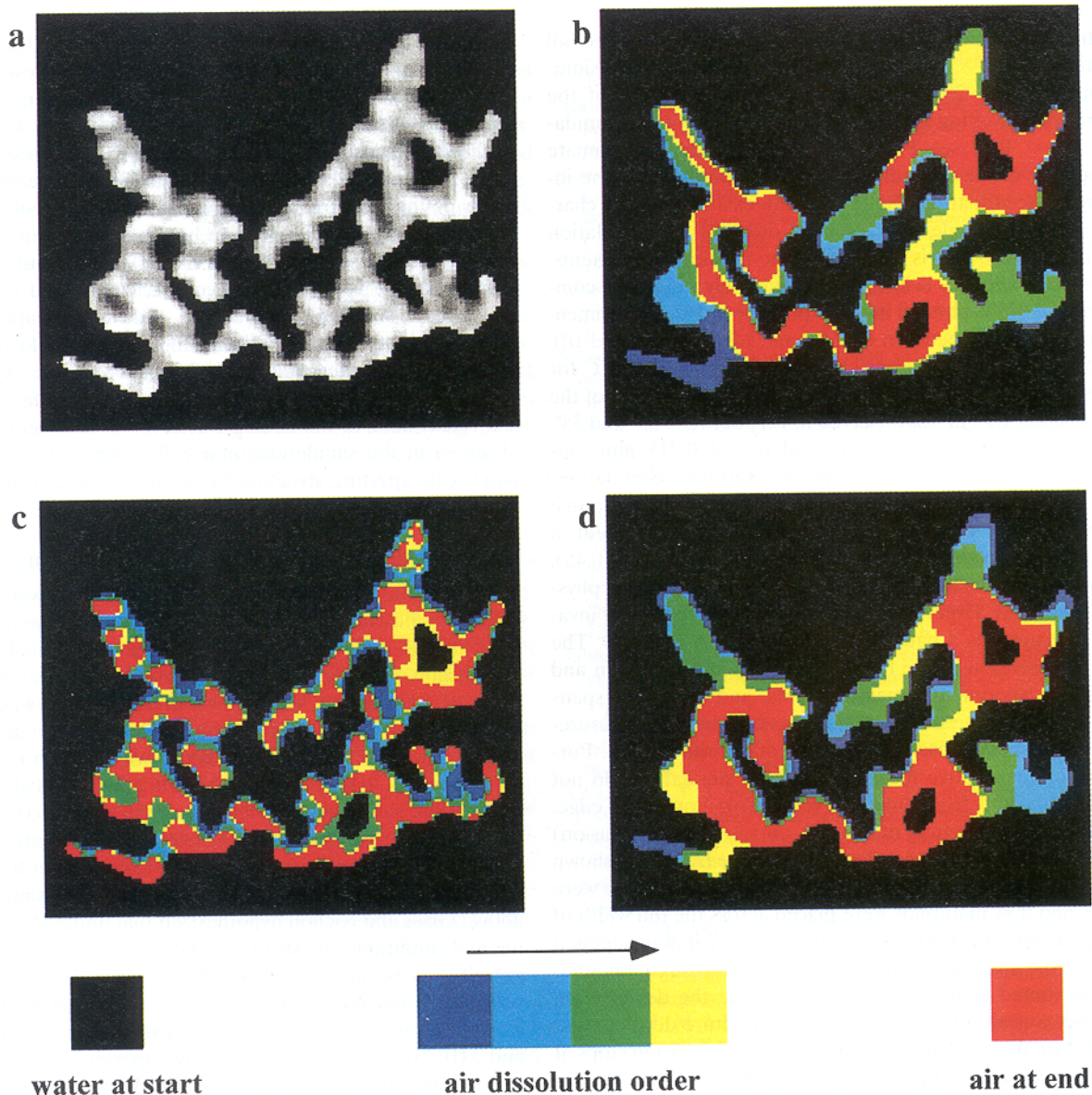


Plate 5. Experimental observation and MIP simulation of nonwetting phase dissolution in a flowing fracture. Entrapped nonwetting phase (air) dissolution into a flowing wetting phase (deaired water) was visualized in the horizontal analog fracture by *Glass and Nicholl [1995a]*. (a) Aperture field as measured using light transmission within a 29×25 mm region encompassing a single nonwetting cluster (gray scale denotes aperture as in Figure 3; black denotes region outside cluster). (b) Order of nonwetting cluster dissolution (replacement of air with water). Apertures where no change in phase occurs are displayed as black (water) and red (air). Apertures where water invades the air as the air dissolves at intermediate times during the experiment are shown as violet, blue, green, and yellow. (c) IP simulation of dissolution sequence on measured aperture field. (d) MIP simulation of dissolution sequence on measured aperture field for $C = 0.45$ (contact angle of 48°).

displacement experiments where phase invasion structure images were collected at low spatial resolution (512×512 pixels, 256 gray levels). Four experiments were conducted at low flow rate, three where water invaded an air-filled fracture and one where air invaded a water filled fracture (data collected in 1991–1992, archived data referenced by *Glass et al. [1997]*). For these experiments the aperture field for any particular experiment was not measured; behavior can be compared to the model results qualitatively and supported by a limited number of quantitative measurements. We then consider the invasion process of entrapped phase dissolution and compare to the

data of *Glass and Nicholl [1995a]*, where both the aperture field and the phase dissolution structures were measured at a resolution identical to that of our MIP simulation (2048×2048 pixel, 4096-gray-level CCD camera) at the time of the experiment; in this case, predicted invasion order can be directly compared to experimental measurements.

5.1. Low-Resolution Phase Displacement Experiments

Experiments considering wetting invasion were performed by slow injection of water into the air-filled horizontal fracture from a point source (center of short edge). Air could escape

the fracture along all edges. The invasion sequence for one of the three experiments is illustrated in Plate 3a. Scale of the full experiment (152×305 mm) is roughly that of the MIP simulations (127.5×292.5 mm). The compact structure of the experimental wetting fronts is notably dissimilar to IP simulations ($C = 0.0$; see Plate 1a), which grossly overestimate entrapment of the defending phase and complexity of the invading phase structure. The IP simulations also display a characteristic length scale that is on the order of the correlation length; a feature that is not seen in the physical experiments. Simulations where r_2 is included more closely reflect the compact nature of the physical invasion process, with the experimental structure falling between C of 0.3 and 1.2 (Plates 1c and 1d).

More explicit comparisons can be made by estimating C for the experimental system. As stated above, contact angle of the experimental system was observed to vary between 35° and 55° . Using measured λ of 0.72 mm and $\langle a \rangle$ of 0.215 mm, this corresponds to a range in C from ~ 0.38 to 0.52. Simulations were conducted over this range of C using a point source inflow boundary condition as was used in the experiment; a representative example, shown in Plate 3b ($\alpha = 48$, $C = 0.45$), demonstrates reasonable qualitative agreement with the physical experiment. Experimental measurements of wetting invasion are shown as a hatched box in Figures 4 and 6–8. The vertical dimension of the box is defined by the minimum and maximum experimental measurements, and the width spans the estimated range in C . In all cases, experimental measurements correspond closely with results of the simulations. Furthermore, quantitative measures of these simulations do not differ significantly from those run with inflow along a full edge.

The slow displacement of water by air (nonwetting invasion) in the single experiment conducted within the fracture is shown in Plate 4. In this experiment the long sides of the fracture were sealed, and flow manifolds were placed across the full width of the upstream and downstream boundaries. Air was supplied slowly to the upstream boundary while the downstream boundary was vented to the atmosphere. Because the downstream boundary was an open reservoir, phase structure development halted once the air spanned the fracture (e.g., invasion stops at breakthrough rather than at satiation). Additionally, the no-flow side boundaries caused the entrapment of large water clusters against the side edges, which in turn restricted the invasion front to a relatively confined backbone in the center portion of the test cell. Even with these differences, it is obvious that the IP process ($C = 0.0$) as shown in Plate 1b differs significantly from the observed phase invasion structure, while those simulations that include r_2 (see Plate 1f) provide a more appropriate representation.

A series of simulations was designed for consistency with the physical experiment; C was varied over a range of 0.38 to 0.52, and no-flow boundary conditions were implemented on the long edges. The invasion structures show good qualitative agreement with the physical experiment. A representative example ($C = 0.45$) is shown in Plate 4b. Quantitative measures for both the simulations and the experiment are plotted in Figures 4 and 6–8 with the single physical experiment displayed as a solid bar spanning the range of estimated C . Simulations specifically designed to reflect experimental conditions are shown as open diamonds joined by a solid line. In all cases the differential response in simulation results between wetting and nonwetting invasion for quantitative structural measures is also seen in experimental results, with lower structural complication and higher areal saturations for wetting

than nonwetting invasion. Measured results show reasonable agreement between model and experiment for areal saturation (Figure 4) and number of clusters (Figure 6); however, in the simulations maximum cluster size (Figure 7) overshoots the experimental observations, while interfacial complexity of the largest cluster is under predicted (Figure 8). In the experiment (Plate 4b) the backbone of the invasion structure spans the width of the fracture near the midpoint. In the simulations (e.g., Plate 4a) a similar feature begins to form but does not fully develop to span the fracture width. As a result, simulations form one very large and compact entrapped cluster. If that cluster had been split by the undeveloped arm of the invading phase backbone, simulation results would be more consistent with the experimental measurements. As noted above, experiments and simulations were run in different physical realizations of the analog fracture; the undeveloped arm observed in the simulations may reflect small differences in large-scale aperture structure between realizations of the analog fracture.

5.2. High-Resolution Gas Dissolution Experiment

The dissolution of entrapped air into a flowing water phase within the baseline fracture was studied by *Glass and Nicholl [1995a]*. The initial entrapment structure was formed by slow air invasion of a water saturated, horizontal fracture (similar to Plate 4) followed by water flow. Entrapped air was subsequently dissolved by switching the flowing phase to deaerated water. Images of the fracture taken with a high-resolution CCD camera (2048×2048 pixels, 4096 gray levels) allowed us to track the shrinkage (dissolution) of the entrapped phase in time. The aperture field for this fracture was measured before the dissolution experiment at a spatial resolution of 0.143 mm per pixel, which is identical to that in our MIP simulations, above. Glass and Nicholl hypothesized that under these experimental conditions, the shrinkage path of individual entrapped gas clusters is simply governed by the same phase invasion processes modeled in MIP. Plate 5 shows the shrinkage of a typical entrapped air cluster along with that predicted by IP and MIP (C of 0.45). MIP is vastly superior to IP at representing the qualitative aspects of shrinking order dynamics. Exact replication of the shrinkage order is not expected because slight errors in the aperture field influence the growth order; however, the compact nature of entrapped phase dissolution seen in the experimental data is well simulated with MIP.

6. Conclusions

Discrepancies between experimental and theoretical results have led to a formulation of modified invasion percolation (MIP) for application to low-capillary number immiscible fluid displacements in horizontal rough-walled fractures. MIP incorporates influences beyond the traditional SP or IP approaches that are either dependent on the local configuration of the invasion front within the fracture (local in-plane curvature and local convergence/divergence within the aperture field) or time (e.g., a dynamic contact angle). In this paper we have focused on understanding the influence of in-plane curvature under conditions where the contact angle is constant in time and space and the influence of local aperture field convergence/divergence is negligible.

We have found that local in-plane interfacial curvature can greatly affect the phase invasion structure in horizontal fractures. The dimensionless curvature number, C , captures the

essence of the interplay between the mean local aperture induced curvature (as parameterized by the mean aperture divided by the cosine of the contact angle) and the mean local in-plane curvature (as parameterized by the spatial correlation length of the aperture field). Where aperture variability dominates (small C), the structure becomes highly complicated and conforms to IP. Where in-plane interfacial curvature dominates (large C), the invading fluid moves across the network from the supply surface with one macroscopic front.

Quantitative measurements show fracture phase saturations, number of clusters and their maximum sizes, and phase structure complication to be highly dependent on C . In addition, these same measures exhibit a differential response to C for wetting and nonwetting invasion that is independent of contact angle hysteresis. We therefore hypothesize macroscopic effective properties or models dependent on underlying phase structure (e.g., pressure/saturation relations, relative permeability, solute dispersion, fracture/matrix interaction) to exhibit strong functional dependency with C that is different for wetting and nonwetting invasion.

Comparison to past experimental data substantiates the MIP model both qualitatively and quantitatively; however, experimental verification across a range of C is yet to be accomplished. Additionally, the systematic variation of the dimensionless aperture field, r_1^* , has yet to be considered either numerically or experimentally. We do expect that as the distribution of r_1^* narrows/widens, the influence of in-plane curvature will increase/decrease, and phase structure behavior with C as seen in Figures 4 and 6–8 will shift to the left/right.

Full evaluation of local interfacial geometry's influence on phase invasion structure within rough-walled fractures requires study of (4) to include both local aperture field convergence/divergence and the spatial/temporal variation of the contact angle. The results of these explorations will yield perturbations around the baseline behavior presented in this paper. Finally, we note that there are many other modifications and extensions that can be made to the current model and analyses. The algorithm for in-plane curvature obviously can be refined. Extensions that allow analysis of other important phase invasion processes in fractures such as gravity/buoyancy-driven flows, fracture/matrix interaction in permeable walled fractures, film flow in micro rough fractures, vapor transport, and the influence of viscous forces at higher capillary numbers are also possible.

Acknowledgments. This work was supported by the U.S. Department of Energy's Basic Energy Sciences Geoscience Research Program under contract DE-AC04-94AL85000. Preliminary model formulation (including buoyancy), simulations, and comparison to data were reported by Glass *et al.* [1997] and partially supported by the U.S. Department of Energy, Office of Civilian Radioactive Waste Management, Yucca Mountain Site Characterization Project Office, under contract DE-AC04-94AL85000. We thank Martin Blunt and Robert Ewing for their constructive reviews of the manuscript.

References

- Blunt, M. J., and H. Scher, Pore-level modeling of wetting, *Phys. Rev. E*, 52(6-B), 6387–6403, 1995.
- Broadbent, S. R., and J. M. Hammersley, Percolation processes, I. Crystals and mazes, *Proc. Cambridge Philos. Soc.*, 53, 629–641, 1957.
- de Gennes, P. G., Wetting: Statics and dynamics, *Rev. Modern Phys.*, 57, 827–863, 1985.
- Deng, Y., I. Chatzis, and F. A. L. Dullien, Computer simulations of gravity driven two-phase immiscible fingering: Effects of gravity and capillarity demonstrated using 2-D network models, *Adv. Water Resour.*, in press, 1998.
- Dussan, V., On the spreading of liquids on solid surfaces: Static and dynamic contact lines, *Ann. Rev. Fluid Mech.*, 11, 371–400, 1979.
- Ewing, R. P., and B. Berkowitz, A generalized model for simulating initial migration of dense non-aqueous phase liquids, *Water Resour. Res.*, 34(4), 611–622, 1998.
- Glass, R. J., Modeling gravity-driven fingering in rough-walled fractures using modified percolation theory, in *High Level Radioactive Waste Management, Proceedings of the Fourth Annual International Conference*, pp. 2042–2053, Am. Nucl. Soc., LaGrange Park, Ill., 1993.
- Glass, R. J., and M. J. Nicholl, Quantitative visualization of entrapped phase dissolution within a horizontal flowing fracture, *Geophys. Res. Lett.*, 22(11), 1413–1416, 1995a.
- Glass, R. J., and M. J. Nicholl, Near drift two-phase flow processes within regionally saturated fractured rock, in *High Level Radioactive Waste Management 1995, Proceedings of the Sixth Annual International Conference*, pp. 212–216, Am. Nucl. Soc., LaGrange Park, Ill., 1995b.
- Glass, R. J., and M. J. Nicholl, Physics of gravity driven fingering of immiscible fluids within porous media: An overview of current understanding and selected complicating factors, *Geoderma*, 70(2-4), 133–163, 1996.
- Glass, R. J., and D. L. Norton, Wetted-region structure in horizontal unsaturated fractures, in *High Level Radioactive Waste Management, Proceedings of the Third Annual International Conference*, pp. 717–726, Am. Nucl. Soc., LaGrange Park, Ill., 1992.
- Glass, R. J., and L. Yarrington, Analysis of wetting front instability using modified invasion percolation theory, *Eos Trans. AGU*, 70, 1117, 1989.
- Glass, R. J., and L. Yarrington, Simulation of gravity fingering in porous media using a modified invasion percolation model, *Geoderma*, 70(2-4), 231–252, 1996.
- Glass, R. J., T. S. Steenhuis, and J.-Y. Parlange, Wetting front instability, 2, Experimental determination of relationships between system parameters and two-dimensional unstable flow field behavior in initially dry porous media, *Water Resour. Res.*, 25, 1195–1207, 1989.
- Glass, R. J., S. H. Conrad, and E. K. Webb, An upscaled buoyant invasion percolation model for use in approaches to delineate subsurface DNAPL location, *AIChE Symp. Ser.*, 306(91), 23–29, 1995a.
- Glass, R. J., M. J. Nicholl, and V. C. Tidwell, Challenging models for flow in unsaturated, fractured rock through exploration of small scale processes, *Geophys. Res. Lett.*, 22(11), 1457–1460, 1995b.
- Glass, R. J., M. J. Nicholl, and V. C. Tidwell, Challenging and improving conceptual models for isothermal flow in unsaturated, fractured rock through exploration of small scale processes, *Rep. SAND95-1824*, 64 pp., Sandia Natl. Labs., Albuquerque, N. M., 1996.
- Glass, R. J., M. J. Nicholl, and L. Yarrington, Development and experimental evaluation of models for low capillary number two-phase flows in rough walled fractures relevant to natural gradient conditions, *Rep. SAND96-2820*, 116 pp., Sandia Natl. Labs., Albuquerque, N. M., 1997.
- Ioannidis, M. A., I. Chatzis, and F. A. L. Dullien, Macroscopic percolation model of immiscible displacement: Effects of buoyancy and spatial structure, *Water Resour. Res.*, 32(11), 3297–3310, 1996.
- Kwicklis, E. M., and R. W. Healy, Numerical investigation of steady liquid water flow in a variably saturated fracture network, *Water Resour. Res.*, 29(12), 4091–4102, 1993.
- Lenormand, R., and C. Zarcone, Role of roughness and edges during imbibition of square capillaries, *SPE Pap. 13264* presented at 59th Annual Technical Conference, Soc. of Pet. Eng., Houston, Tex., Sept. 16–19, 1984.
- Lenormand, R., and C. Zarcone, Invasion percolation in an etched network: Measurement of a fractal dimension, *Phys. Rev. Lett.*, 54(20), 2226–2229, 1985.
- Meakin, P., A. Birovljev, V. Frette, J. Feder, and T. Jossang, Gradient stabilized and destabilized invasion percolation, *Physica A*, 191, 227–239, 1992.
- Mendoza, C. A., Capillary pressure and relative transmissivity relationships describing two-phase flow through rough-walled fractures in geologic materials, Ph.D. dissertation, Dep. of Earth Sci., Univ. of Waterloo, Waterloo, Ontario, Canada, 1992.
- Nicholl, M. J., and R. J. Glass, Wetting phase permeability in a partially saturated horizontal fracture, in *High Level Radioactive Waste*

- Management, Proceedings of the Fifth Annual International Conference*, pp. 2007–2019, Am. Nucl. Soc., LaGrange Park, Ill., 1994.
- Nicholl, M. J., R. J. Glass, and H. A. Nguyen, Gravity-driven fingering in unsaturated fractures, in *High Level Radioactive Waste Management, Proceedings of the Third Annual International Conference*, pp. 321–331, Am. Nucl. Soc., LaGrange Park, Ill., 1992.
- Nicholl, M. J., R. J. Glass, and H. A. Nguyen, Small-scale behavior of single fingers in an initially dry fracture, in *High Level Radioactive Waste Management, Proceedings of the Fourth Annual International Conference*, pp. 2023–2032, Am. Nucl. Soc., LaGrange Park, Ill., 1993a.
- Nicholl, M. J., R. J. Glass, and H. A. Nguyen, Wetting front instability in initially wet fractures, in *High Level Radioactive Waste Management, Proceedings of the Fourth Annual International Conference*, pp. 2061–2070, Am. Nucl. Soc., LaGrange Park, Ill., 1993b.
- Nicholl, M. J., R. J. Glass, and S. W. Wheatcraft, Gravity-driven infiltration instability in initially dry nonhorizontal fractures, *Water Resour. Res.*, 30(9), 2533–2546, 1994.
- Prat, M., Percolation model of drying under isothermal conditions in porous media, *Int. J. Multiphase Flow*, 19(4), 691–704, 1993.
- Pruess, K., and Y. W. Tsang, On two-phase relative permeability and capillary pressure of rough-walled rock fractures, *Water Resour. Res.*, 26(9), 1915–1926, 1990.
- Pyrak-Nolte, L. J., N. G. W. Cook, and L. R. Myer, Stratified percolation model for saturated and unsaturated flow through natural fractures, in *High Level Radioactive Waste Management, Proceedings of the International Topical Meeting*, pp. 551–558, Am. Nucl. Soc., LaGrange Park, Ill., 1990.
- Schwille, F., *Dense Chlorinated Solvents in Porous and Fractured Media*, Lewis, Chelsea, Mich., 1988.
- Wilkinson, D., and J. F. Willemsen, Invasion percolation: A new form of percolation theory, *J. Phys. A Math. Gen.*, 16, 3365–3376, 1983.
-
- R. J. Glass and L. Yarrington, Flow Visualization and Processes Laboratory, Sandia National Laboratory, Albuquerque, NM 87185-1345. (e-mail: rjglass@sandia.gov)
- M. J. Nicholl, School of Geology, Oklahoma State University, Stillwater, OK 74078.

(Received June 23, 1997; revised June 30, 1998; accepted July 1, 1998.)